

Development of Fringe Image Processing Algorithms for Tomographic Reconstruction of Temperature Field in an Axisymmetric Medium

Ibtihal Mohammed Khaleel

Al Farahidi University, Iraq

DOI:

<https://doi.org/10.47134/pslse.v2i1.319>

*Correspondence: Ibtihal Mohammed Khaleel

Email:

Ibtihal.mohammed@uofarahidi.edu.iq

Received: 23-10-2024

Accepted: 23-11-2024

Published: 24-12-2024



Copyright: © 2024 by the authors. Submitted for open access publication under the terms and conditions of the Creative Commons Attribution (CC BY) license (<http://creativecommons.org/licenses/by/4.0/>).

Abstract: *This work is part of the development of algorithms and digital tools for the tomographic reconstruction of the (3D) temperature field from images resulting from thermal metrology based on two optical techniques (Moire deflectometry and holographic interferometry). It is intended not only for digital scientists and image processing specialists but also for researchers and practitioners in instrumentation and measurement by non-invasive techniques in general and in thermal metrology by optical techniques in particular. Tomography by optical techniques of axisymmetric transparent media, the main subject of application of this thesis, is a perfect example of an imaging system based on an elementary mathematical property (the Abel transform and its inverse in this case). This property comes up against in its practical application the hypersensitivity to noise and problems due to the intrinsic characteristics of this transform. However, the study of transparent media such as air in our case, which does not present any radiative, absorption or diffusion properties, makes the images resulting from optical techniques unusable only after a treatment which precedes the inverse calculation of the Abel transform. This treatment thus limiting the development of 3D imaging requires special attention. Furthermore, the tomographic reconstruction of the temperature field of such an environment will be done in two processing parts, the first of which will focus on the analysis of mud figures, while the second is dedicated to solving the inverse problem generated by the Abel transform.*

Keywords: *Fringe Image Processing Algorithms, Tomographic Reconstruction, Temperature Field, Axisymmetric Medium*

Introduction

We discuss the process of extracting the phase-encoded in the synthetic fringe patterns, This process is referred to in the jargon of digital scientists as fringe analysis, Generally, this process involves two steps, the first of which is the extraction of the phase itself. The second step will focus on the possible unfolding of this phase.

We will pay special attention to the different algorithms for extracting the wavelet crest, which is necessary to measure the phase from optical images. Three algorithms are considered: the direct maximum algorithm, the Liu algorithm, the cost function algorithm, and the Marseille Group algorithm to find the most adequate and robust algorithm. Then,

we dissect the phase unfolding problem To do this, four algorithms are tested and compared, namely the Itoh 1D algorithm, the Itoh 2D algorithm, the Goldstein 2D algorithm and the Arealillo Herráez algorithm (Liu, 2024b).

All the algorithms presented in this extension are programmed under Matlab. Their validation was judged by considering the two quality criteria, namely the PSNR and/or the MES.

Literature Review

We have chosen to test the algorithms that we develop in this chapter on an image of synthetic fringes The phase that is at the origin of these fringes is calculated numerically using a two-dimensional analytical expression This procedure is widely used in the literature for the numerical validation of algorithms for fringe analysis (Liu, 2020).

Moreover, this choice spares us from the complexity and the high cost of simulations in realistic configurations (Sharma, 2024).

In principle, one can simulate a fringe pattern from any two-dimensional distribution representing the phase shift in interferometry or the deflection angles in moiré deflectometry It is sufficient simply to formulate a mathematical expression for these quantities in the form of a function of two variables Thus, we consider as an example the following analytical expression:

$$\begin{aligned} \varphi(y,z) = & 3(1 - y)^2 \exp[-y^2(z+1)^2] \\ & -10(y/5 - y^3 - z^5) \exp(-y^2 - z^2) \\ & \exp[-(y+1)^2 - z^2] \quad (1) \end{aligned}$$

Figure 1. illustrates the graphical representation of the distribution of (y, z) according to a sampling of 512x512 pixels

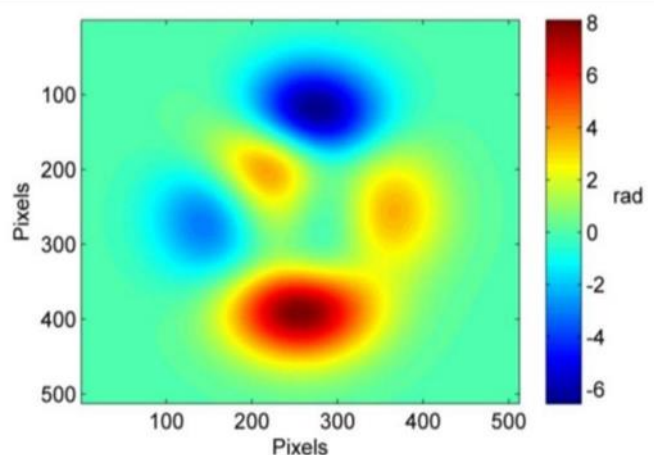


Figure 1. Theoretical phase image sampled at 512x512 pixels.

We inject expression (1) as a phase term into the fringe equation $I(y, z)$ which we recall here:

$$I(y,z) = \text{Im}(y,z) + V(y,z) \cos [2\pi\nu_0 y + \varphi(y,z)] \quad (2)$$

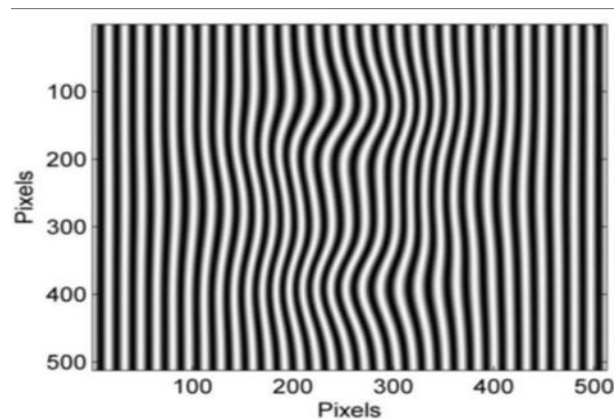


Figure 2. Synthetic fringes with $Im = 0$, $V = 1$, $v_0 = 0.08$.

The result of this calculation gives the fringe image shown in Figure 2.

Figure 3. shows the same fringe image but this time affected by multiplicative speckle noise with an average grain size of 5×5 pixels.

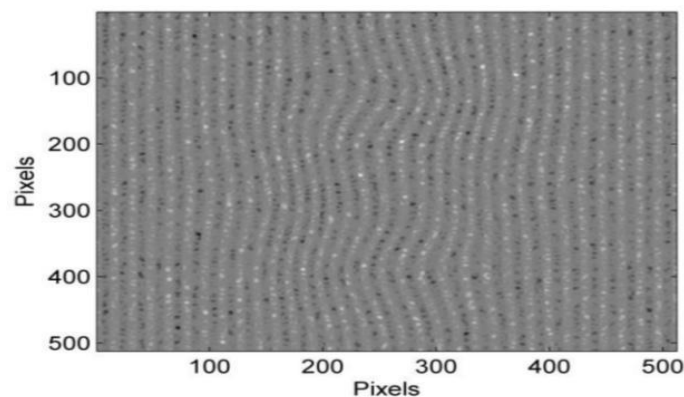


Figure 3. Noisy fringe image

Methodology

The analysis of an optical image with a view to reconstructing the temperature field which gave rise to it begins first of all with the extraction of the phase.

This step is composed of a sequence of mathematical and numerical operations. The precision and speed of the phase measurement are closely linked to the choice of algorithms and their parameters (Federico, 2021).

Figure 4 illustrates the sequence of all the operations and algorithms that can be used to arrive at the distribution of the unknown phase. Our goal through the following story is to find and justify the best procedure for the processing of an optical image by the wavelet transform technique (Liu, 2024a).

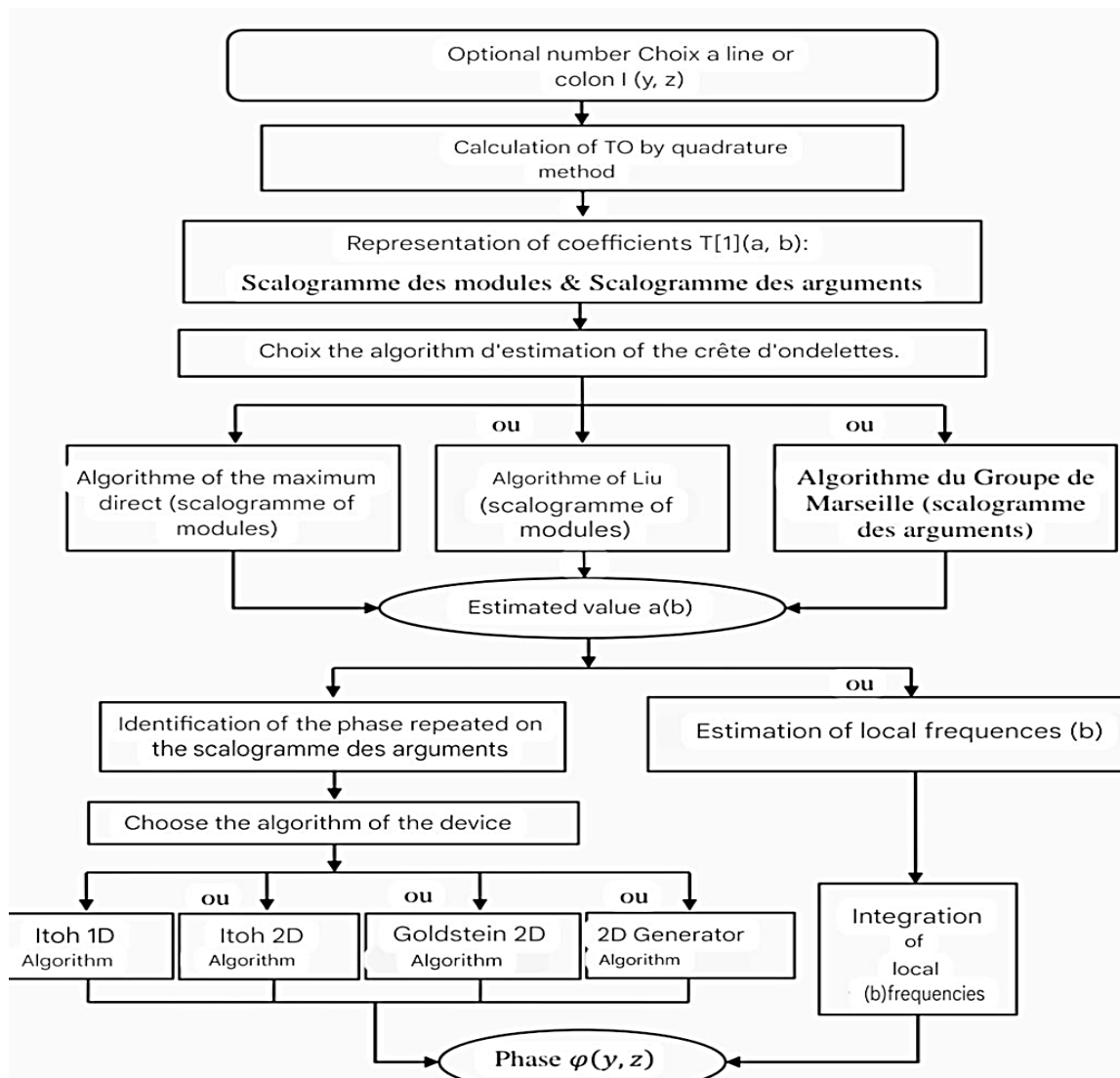


Figure 4. Illustrative flowchart for fringe analysis

Calculation of scalograms

To better illustrate how this approach works, consider Figure 5, which plots the intensity on line 400 of the simulated fringe image (Figure 2).

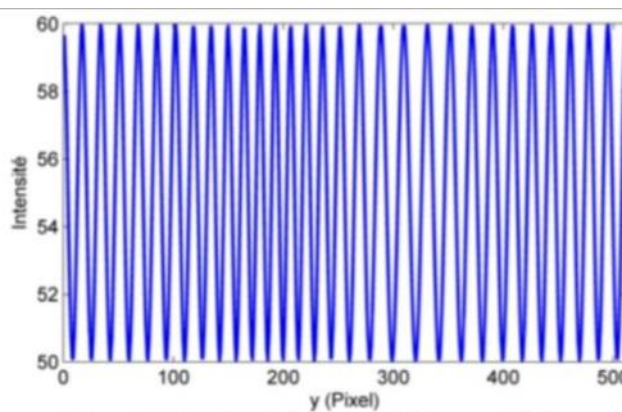


Figure 5. Intensity profile 1(y, z = 400).

After calculating the wavelet transform of this line, we can easily access the two amplitude and phase scalograms (Figure III-6). We have chosen to work with the complex Morlet wavelet, which is commonly used.

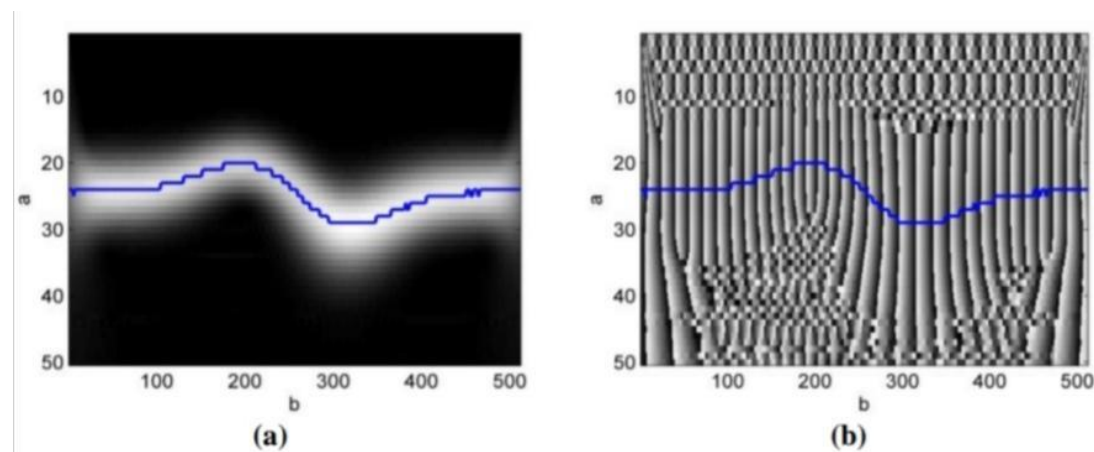


Figure 6. Images (a) and (b) represent respectively the scalogram of the modules and the scalogram of arguments.

The wavelet crest profile can easily be observed on the scalogram of the modules (Figure 6a) in the form of a clear band. The calculation of the TO can be interpreted as a calculation of the correlation coefficients between the signal and the different daughter wavelets (Junne, 2024). These coefficients take values in the module as large as the daughter wavelet, and a portion of the signal is similar (light area on the modulus scalogram). In other words, the TO modulus is maximal when a daughter wavelet has an analysis frequency very close to the local frequency of the signal. This causes the appearance of a peak that gives access to the variations of the phase and frequency of the signal (Bracewell, 2000)

Estimation of the wavelet crest

In a fringe analysis process using TO, the detection of the wavelet crest is a crucial step. For this purpose, we will implement and test three algorithms, namely: the direct maximum algorithm, the Liu algorithm, and the Marseille Group algorithm. Their reliability will be evaluated by considering the PSNR quality criteria for each algorithm (Chan, 2021).

Direct maximum algorithm

Test on a noise-free image

This algorithm is quite simple to program. The extraction of the set of points forming the wavelet crest is done at the level of the scalogram of the modules (Figure 6a). We determine the coordinates (aC, b) of the maximum value of each column in the module matrix as illustrated in Figure 7 (Maddah, 2024). The value of the corresponding phase is extracted from the argument matrix by a simple identification. The repetition of these two

operations on all the columns of the module matrix allows us to draw the profile (Figure 8a) of the folded phase ((Dribinski, 2020)

In order to demodulate the entire fringe image, this process will be repeated for all the lines Appendix (B) represents the implementation of the MD algorithm. The result is a map of the folded phase represented in 256 grey levels, as shown in Figure 8 b. To qualitatively ensure the result obtained, we recalculated the fringes by introducing the phase of the folded phase in formula (2). The result of this operation is illustrated in Figure III-8 e, which is a faithful duplicate of the initial fringe image (Figure 2)

This qualitatively demonstrates the ability of the MD algorithm to demodulate the simulated fringe pattern without noise (Choi, 2024).

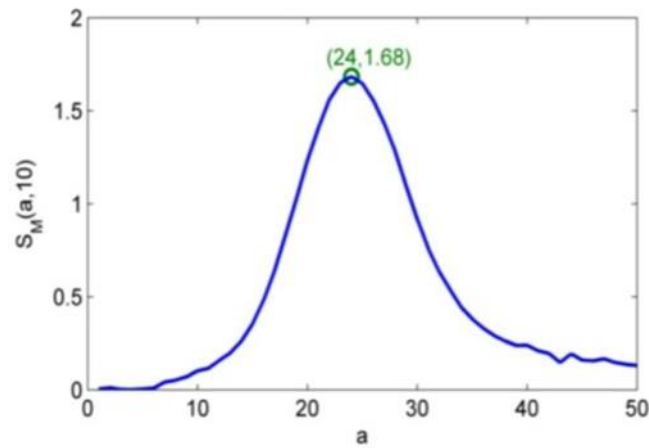


Figure 7. Profile of the variation of the values of the tenth column of the TO amplitude scalogram

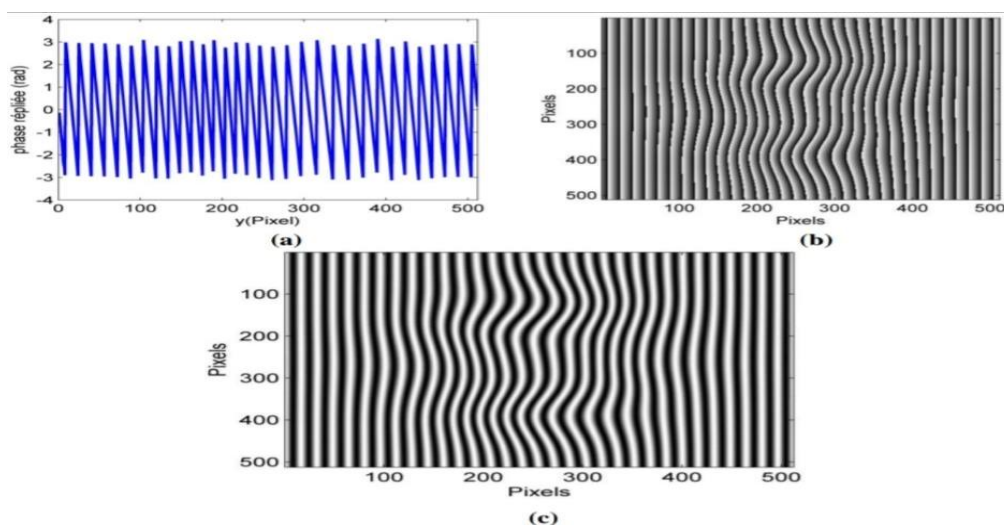


Figure 8. (a) Folded phase corresponding to the intensity line z 400. (b) mapping of the folded phase. (c) image of the fringes reconstructed from the folded phase.

Test on a noisy image

To show the limitations of this algorithm, we this time use the noisy fringe image in Figure 3. The result of the fringe demodulation by the MD algorithm is illustrated in Figure 9. Overall, the recalculated image is sharper than the noisy image in Figure 3. We can then understand the ability of the TO technique to filter the fringes and overcome the effects of speckle noise (Lv, 2024).

However, we observe in some areas singular points on the fringes appearing in the form of stripes (areas circled in red in Figure 9) These points correspond to the best correlation of the daughter wavelets with the noise instead of the sought signal The MD algorithm, which only detects the absolute maximum, does not allow to bypass these singular points. Consequently, a more selective algorithm of the points forming the peak proves to be more adequate (Ignjatovic et al, 2019).

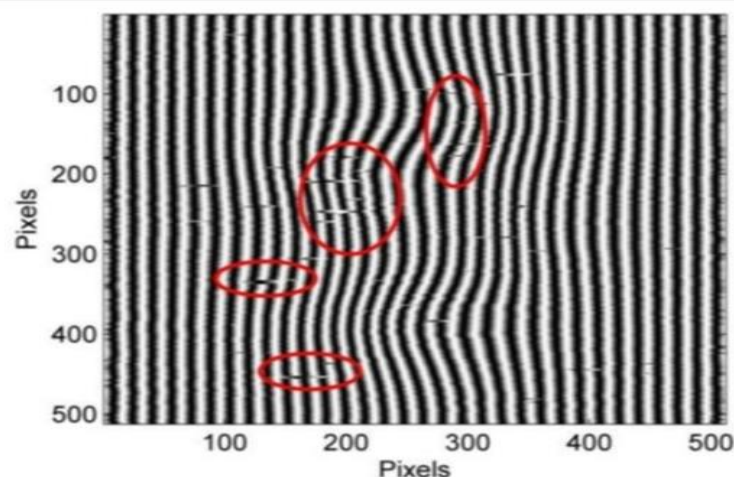


Figure 9. Image of the recalculated fringes showing some areas of singular points.

Liu's algorithm

Wavelet crest detection using dynamic programming by minimizing the cost function was introduced by Liu, The objective is to correct the anomalies inherent in the systematic application of the absolute maximum search algorithm to estimate the wavelet crest The solution proposed by Liu is to consider jointly with the absolute maximum all the relative maxima of the modulus of the wavelet transform To fix the ideas, let us apply this algorithm on line 400 of the noisy interferogram represented by **Figure 3**

All the results of this example are illustrated in Figure 11 For each candidate likely to be part of the peak, we evaluate the cost function or "cost," whose expression is the following: (Asaki et al, 2019).

$$\text{Cost}[f(b),b] = - \int_b \{S_m[f(b),b] \}^2 db + \int_b [df(b) / db]^2 ad \quad (1.3)$$

where f is a function describing the evolution of the scales a as a function of the translation parameter b . $Sm[f(b), b]$ is the module value of the TO to the candidate $(f(b), b)$. The choice between the relative maximums of the TO module of the column considered will be made by looking for the value $a_c(b)$ for which the function $Cost[f(b), b]$ is minimal. The discretization of equation (3) with a step $\Delta b = 1$ allows us to arrive at the following simplified expression (Chamaco, 2019).

$$Cost(n, b + 1) = \min_m (cost(m, b) - \{SM[f(m), b + 1]\}^2 + [n - m]^2) \quad (1.4)$$

where n and m represent two indices which respectively scan the positions of the relative maxima of column b and column $b + 1$.

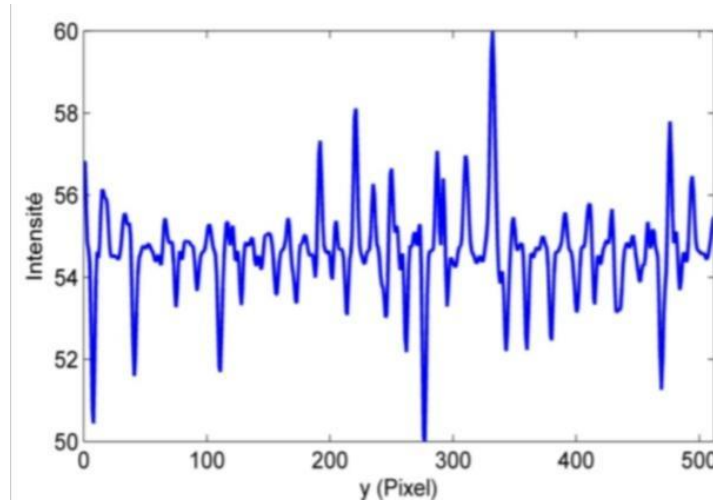


Figure 10. Intensity profile ($z = 400$) of the fringe image (Figure 3)

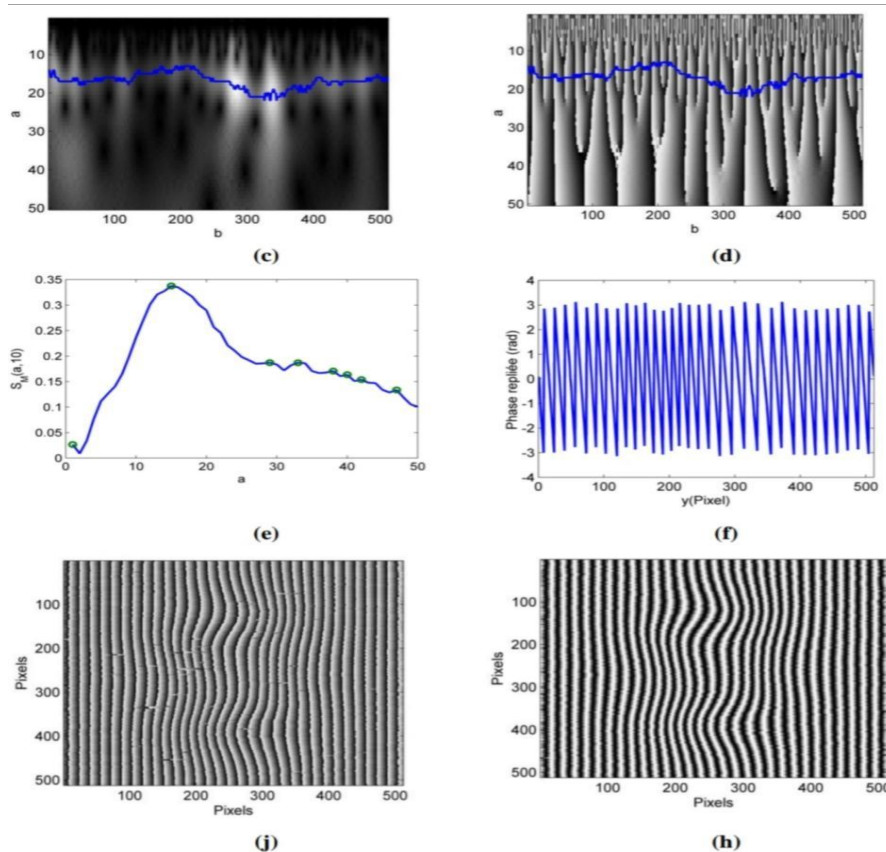


Figure 11. (a) intensity profile on the line $z = 400$. (c) Amplitude scalogram. (d) Argument scalogram. (e) Scale evolution profile for column $b = 10$ where the maxima are indicated by circular patterns. (f) The folded phase profile of the line $z = 400$. (j) Folded phase map. (h) Image of the recalculated fringes.

We start by determining the candidates that will form the peak using the Matlab findpeaks function The result of this operation applied to the example treated is given in Table 1 for the coordinates $(f(b), b)$ and in the table for the $SM[f(b), b]$ modules (Goharkhaha et al, 2020).

Then, we proceed to calculate the cost function for each candidate to draw up the tables (Table 1 & Table 2) The last step consists in identifying the candidate and therefore the point of the sought peak giving rise to the minimum cost on each column (see the values in bold and italics in Table 3).

All the steps necessary for the implementation of Liu's algorithm are illustrated in Appendix (B).

Table 1. Coordinates of the candidate for the formation of the ridge.

	b = 1	b = 2	...	b =10	...	b = 256	...	b = 512
a	0	0.0044		172.2643		148.7055		140.3233
	0	0.0610		4.1511		132.6524		140.3217
	0	0.0604		18.7361		117.6514		104.3206
	0	0.0268		2.7361		52.5457		208.3381
	0	0.9762		9.7454		143.1917		224.3379
	0	8.9835		13.7503		140.1938		228.3379
	0	0.0178		17.8173		160.2108		240.3379
	0	0.9857		30.8312		181.2259		
	0	-						

Table 2. Values of relative maxima.

	b = 1	b = 2	...	b =10	...	b = 256	...	b = 512
a	0.0659	0.0662		0.0265		0.0085		0.0439
	0.2227	0.2469		0.3375		0.0326		0.0449
	0.2257	0.2458		0.1871		0.0444		0.0556
	0.1614	0.1638		0.1869		0.2349		0.0153
	0.1678	0.1544		0.1706		0.1445		0.0166
	0.1485	0.1286		0.1635		0.1395		0.0171
	0.1429	0.1334		0.1537		0.1086		0.0182
	0.1253	0.1194		0.1336		0.0881		
	0.1113	0.0662						

Table 3. Costs relative to all candidates to form the crest.

	b = 1	b = 2	...	b = 10	...	b = 256	...	b = 512
a	4	4		1		1		9
	14	14		15		5		11
	16	16		29		8		17
	29	31		33		17		31
	31	35		38		33		35
	34	40		40		36		37
	37	43		42		42		39
	43	47		47		47		
	46	4						

Marseille Group Algorithm

Like the moduli scalogram, the second space-frequency representation of the wavelet transform is also exploitable. This idea was first proposed by Delpar and implemented in the form of an algorithm called the Marseille Group algorithm. The latter is based on the fact that when the frequency $f = fc/a$ of the analyzing daughter wavelet $\Psi_{a,b}$ is close to the frequency f_s of the signal, then the rate of variation of the phase of the TO $\partial\Phi\Psi(a,b)/\partial\Phi$ coincides with f for the points of the scalogram of the arguments belonging to the crest. The steps of this algorithm are illustrated in Appendix (B). [10] (Zhong et al, 2019)

The computations are initialized by a scale value a_p . A new frequency f_1 is then determined by calculating the quantity $\partial\Phi\Psi(a_0,b)/\partial d$. The corresponding scale value $a_1 = f_0/f_1$ is then used to find $f_2 = \partial\Phi\Psi(a_1,b)/\partial\Phi$.

The computations are stopped when the relative error $|a_{i+1} - a_i|/a_i$ between two successive iterations i and $i + 1$ becomes less than the fixed tolerance. Once $f_s(b)$ has been found, the algorithm continues at point $b + 1$ with this time a , $f_c/f_s(b)$. Taking as an example the noise-free image (Figure 2), the estimation of the peak using the Marseille Group algorithm is illustrated in Figure 12, representing the scalogram of the arguments. The plot of this estimated peak on the scalogram of the modules allows us to detect a clear shift in relation to its position visually marked by a light band (see Figure 12 b). (Jackson et al, 2021).

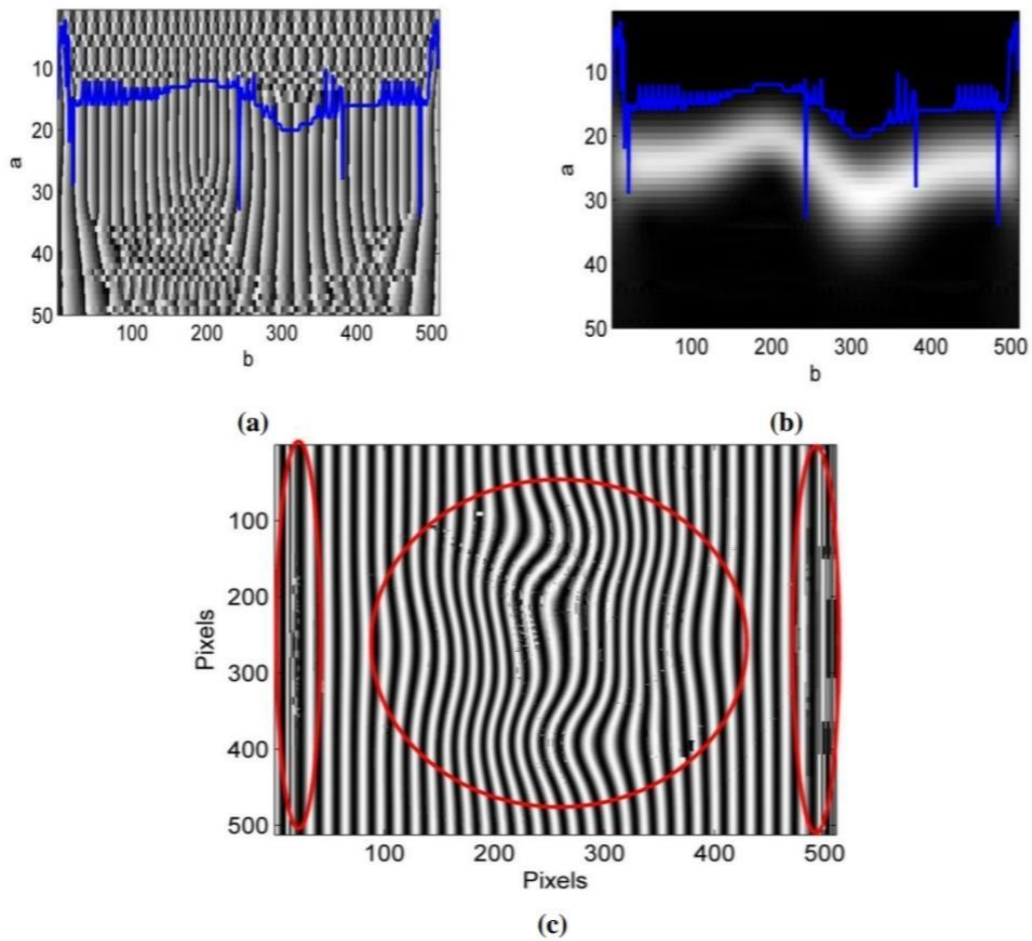


Figure 12. (a) Scalogram of the TO arguments. (b) Scalogram of the modules showing the crest. (c) Reconstructed fringe image

Result and Discussion

In order to perform a quantitative comparison between the three demodulation algorithms, we calculated the PSNR and determined the temporary complexity of each algorithm. This robustness test will be performed on fringe images affected each time by a speckle noise of grain size varying between 1×1 and 5×5 pixels (Yu, 2024).

The figure reports the PSNR corresponding to each algorithm for a noise-free image and five images noisy by a speckle of size respectively 1×1 , 2×2 , 3×3 , 4×4 , and 5×5 . As a comparison, fringe images reconstructed on the basis of 5×5 noise by the three algorithms are illustrated in Figure 14 (Li, 2024).

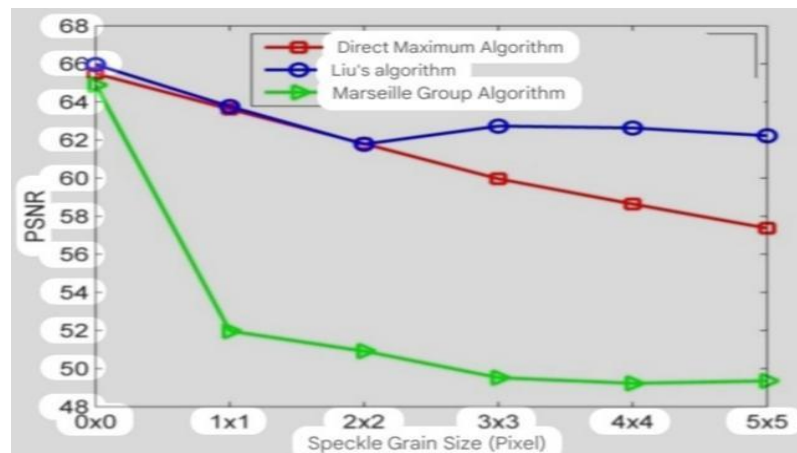


Figure 13. Evolution of the PSNR quality criterion as a function of the speckle gain size for the three wavelet crest estimation algorithms.

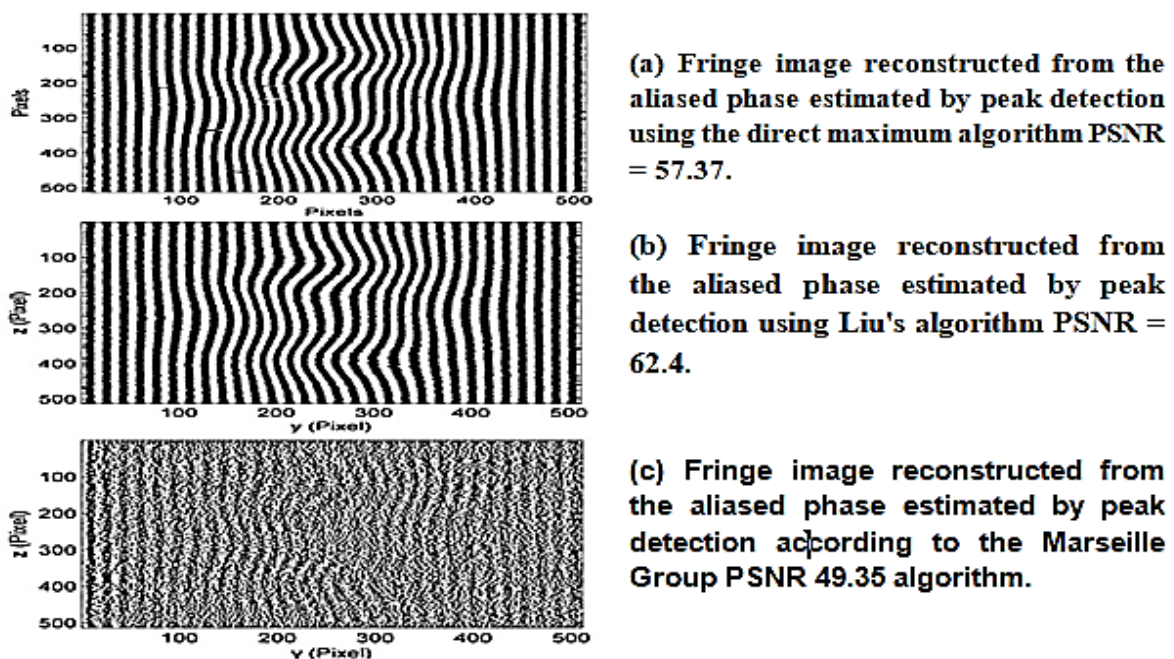


Figure 14. The reconstructed images according to the three peak detection algorithms, respectively, from top to bottom, the direct maximum algorithm, the Liu algorithm, and that of the Marseille group.

We have verified that whatever the algorithm when the size of the speckle gains increases, the PSNR between the original image and the estimated image will decrease, but according to different issues (Zarch, 2024).

Looking at Figure 13, we see that in the absence of noise, the three algorithms are very comparable since their respective PSNR values are in the same range. In the presence of noise, the PSNR values of each algorithm deviate, thus demonstrating a difference in

sensitivity to noise, Moreover, the direct maximum algorithm remains the easiest to implement and the least demanding in memory and computing time. It also provides a good result (see Figure 14 a) in comparison with the Marseille Group algorithm. The latter generates a more marked loss in PSNR as the size of the speckle grains increases (see Figure 13 and Figure 14 c) It is also important to mention that this algorithm has major drawbacks related to the choice of tolerance and the initialization value a_0 . Indeed, low tolerance values can cause a divergence of the algorithm (especially in case of noise) or in the best case, an increase in the calculation time without improving the accuracy of the results. In addition, the choice of the initialization value a_0 remains a weak point of this algorithm. Indeed, the value of a_0 can be responsible for the appearance of edge effects, as shown in Figure 12(c).

The solution we have considered to remedy this problem is to initialise the calculations by a value of a_0 taken from the scalogram of the modules where the peak is clearly observable as a clear band. These drawbacks constitute an obstacle to the automation of the Marseille Group algorithm for the extraction of the phase or the filtering of images in real time.

Liu's algorithm remains probably the most robust, as justified by the evolution of the PSNR (Figure 13) , The direct maximum algorithm gives a PSNR close to that obtained by Liu's algorithm for speckle grain sizes smaller than 2×2 pixels On the other hand, a clear difference appears between these two algorithms when the speckle grain size exceeds 2×2 pixels. This same observation was reported by Liu et al. for moiré fringe images .

Moreover, Liu's algorithm is not perfect. Indeed, when the noise becomes too large the number of candidates to form the optimal peak increases, which makes it difficult to minimize the cost function and causes an increase in time complexity Of course, these two drawbacks make real-time processing of fringe images for thermal metrology difficult.

Conditioning and choice of the wavelet

Whatever the algorithm adopted for the exploitation of the TO scalograms, the user intervention remains minimal and only slightly affects the quality of the result in comparison with the demodulation by the Fourier transform. The supervision of the algorithm is limited to the following two data:

1. The choice of the scale interval $[A_{min}, A_{max}]$ as well as its sampling step A_a to scan both the low and high frequencies of the analysed signal.
2. The choice of the mother wavelet and its parameters.

The choice of the scale interval can be done by trial and error or by the preliminary calculation of the frequency spectrum of the signal in order to designate a useful frequency band $[f_{min}, f_{max}]$ and to link it to the scale interval $[a_{min}, A_{max}]$. Rigorously establishing such a relationship can be done for certain mother wavelets, such as the Morlet wavelet.

Indeed, this wavelet has a very explicit central frequency f_c The scales can then be expressed exactly as a function of this frequency and those of the signal. As for determining the appropriate sampling step A_a , the aim is to optimise the calculation time on the one hand and to reduce the aliasing effect in the peak on the other hand, as we will see later.

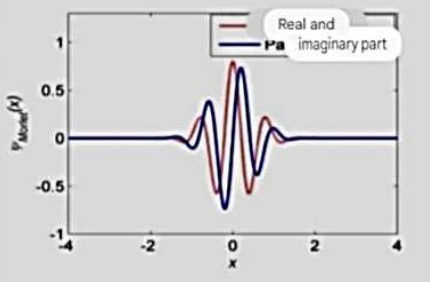
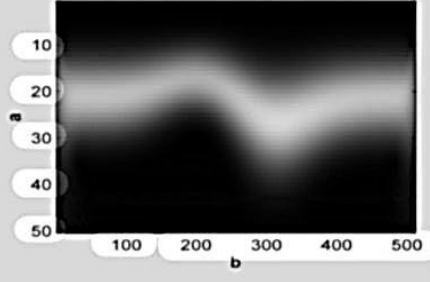
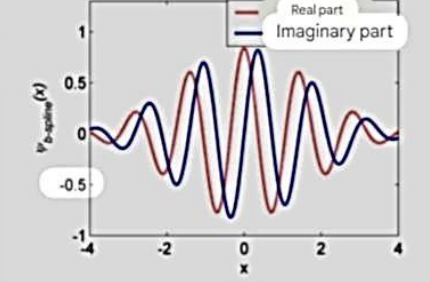
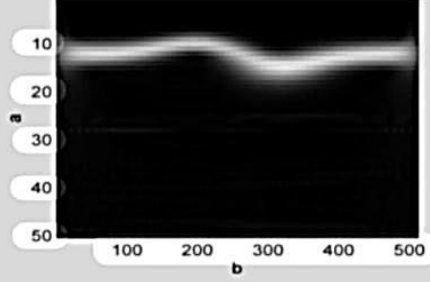
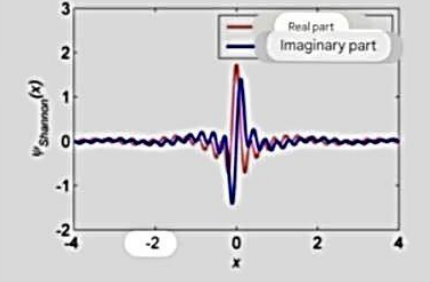
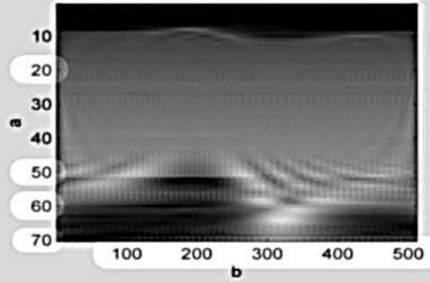
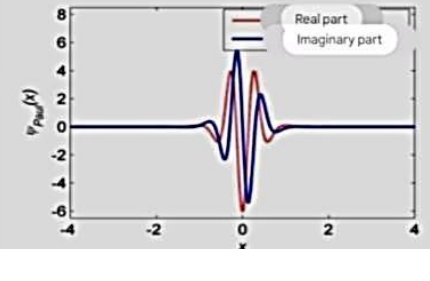
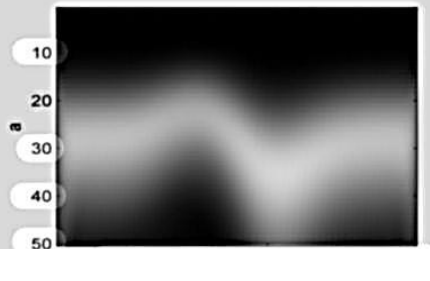
For the second point, the choice of the mother wavelet is decisive. Given the spectacular development of signal processing by wavelet theory, there are currently a variety of analyzing mother wavelets; however, there is no rigorous rule that facilitates the choice between them. Let us say that the general approach consists of testing a few of them to decide the mother wavelet suitable for the processed signal. In the context of this thesis, we have chosen to test seven mother wavelets to analyse fringe images.

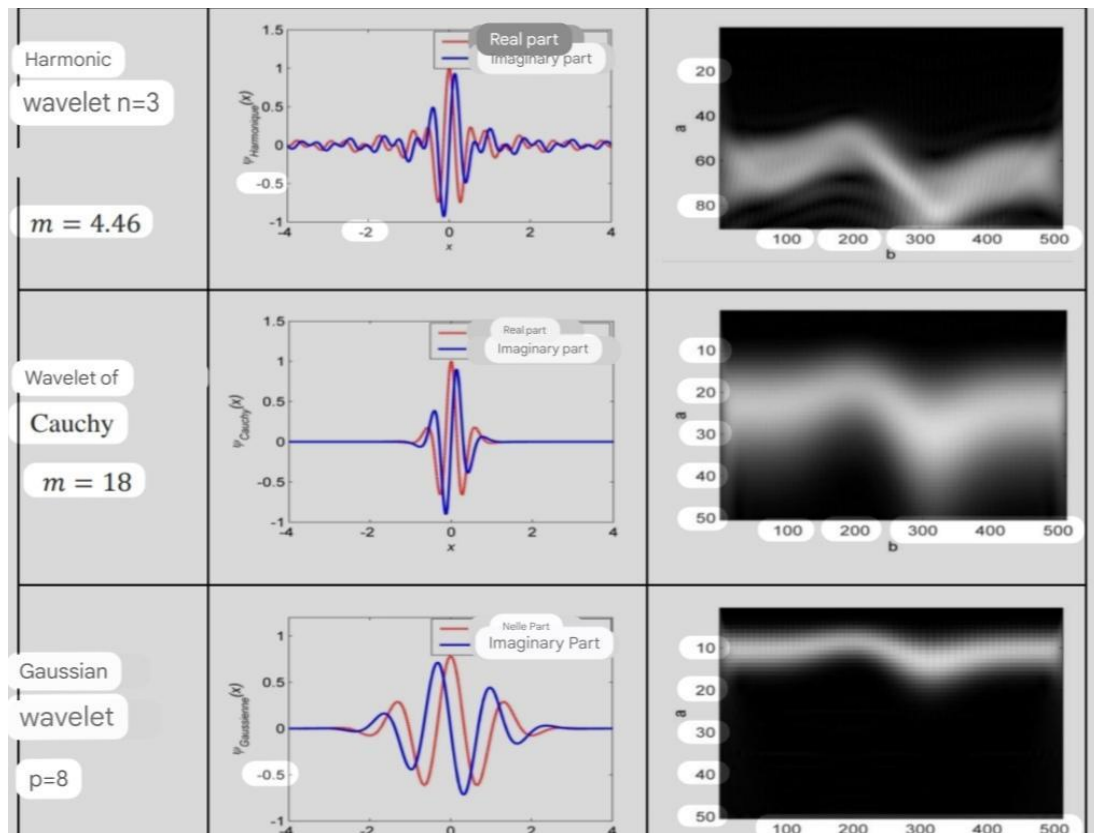
The shapes of these wavelets and their scalograms of the respective modules are shown in Table 4. We compared the results of each of these mother wavelets.

$$\begin{aligned}\psi_{Morlet}(x) &= \frac{1}{(f_b^2 \pi)^{1/4}} \exp(i2\pi f_c x) \exp\left(\frac{-x^2}{2f_b^2}\right) \\ \psi_{b-spline}(x) &= \sqrt{f_b} \exp(i2\pi f_c x) \left[\text{sinc}\left(\frac{f_b x}{m}\right) \right]^m \\ \psi_{Shannon}(x) &= \sqrt{f_b} \exp(i2\pi f_c x) [\text{sinc}(f_b x)] \\ \psi_{Paul}(x) &= \frac{2^n n! (1 - ix)^{-(n+1)}}{2\pi \sqrt{\frac{(2n)!}{2}}} \\ \psi_{harmonic}(x) &= \frac{\exp(i2n\pi x) - \exp(i2m\pi x)}{i2\pi(n - m)x} \\ \psi_{Cauchy}(x) &= \frac{i}{(x + i)^{m+1}} \\ \psi_{Gaussian}(x) &= \frac{d^p [C_p \exp(-ix) - \exp(-x^2)]}{dx^p}\end{aligned}$$

For this, we considered two criteria, one qualitative and the other quantitative, to decide on these wavelets regarding the adequacy of the processed signal. The sharpness, applicability, as well as shape of the peak, must be taken into consideration by a simple visualization of the scalogram of the modules. Then, we compare the PSNR between the recalculated image and the reference one.

Table 4. Comparison between the different mother wavelets used for calculating the wavelet transform of the intensity line located at $z = 400$ pixels of the image of the theoretical fringes in **Figure 2**. The first column shows the name of the mother wavelet and its different parameters; the second is reserved for graphical representations of its real and imaginary parts, while the last presents the scalograms of the moduli of the crest.

Name and parameters of the analyzing wavelet	Profile of the real and imaginary parts	Scalograms of modules
Wavelet of Morlet $f_c = 1.7$ $f_b = 0.5$		
Wavelet b-spline $f_c = 0.7$ $f_b = 0.7$ $m = 5$		
Shannon wavelet $f_c = 3, f_b = 2$		
Wavelet of Paul $n = 5$		



Phase unfolding

Position of the problem

In this extension, it is not the numerical study or the way of implementing the unfolding algorithms that concerns us, but rather the practical analysis of the unfolding problem (1D or 2D). We will be content with an overview of the principle of each algorithm in focusing on the discussion of the quality of the results it provides. We will consider the ability of each algorithm to unroll the phase suitably and fairly, freeing itself from singularities that may arise due to the presence of obstacles (heating objects, for example) or parasitic spots outside the fringe figures (diffraction, optical aberrations, speckle, etc.).

We also mention the singularity resulting in particular from the addition of an additional poorly chosen reference phase. In other words, we will examine the ability of the algorithm to distinguish between a "true discontinuity" and a "false discontinuity." We will see that certain 2D algorithms make it possible to circumvent these singularities without affecting the precision of the unrolling of the phase.

Itoh Condition

All the algorithms used in this thesis are based on the Itoh algorithm, which is local. The most natural approach to unfolding the phase is to proceed pixel by pixel. We denote by $\varphi_w(n)$ and $\varphi_u(n)$ the discrete phases respectively discontinuous and continuous, and n the pixel number. To remove the discontinuities of $\varphi_w(n)$, we must add or subtract 2π at each point, giving rise to a sudden variation of the phase.

However, the continuous phase can itself contain sudden variations between two pixels due to the singularity problems mentioned above. These variations may interfere with the unfolding algorithm and thus alter the result. The Itoh condition stipulates that between two adjacent pixels, we cannot go from a dark fringe to a bright fringe and vice versa. The following relation translates the Itoh condition:

$$|\varphi_v(\eta) - \varphi_v(\eta - 1)| < \pi \quad (12)$$

Failure to verify condition (12) is commonly referred to as a violation of Itoh's condition. It is worth pointing out a certain absurdity of this condition since in reality the continuous phase is not known a priori.

Unfolding algorithms

For the study of the unfolding problem, several algorithms exist in the literature. We have selected three: Itoh's algorithm Goldstein's and Arevalillo Herráez's

ID algorithm

Itoh's algorithm can be summarized by saying that phase unfolding is obtained by integrating the discontinuous phase. This procedure can be performed numerically using the following algorithm:

$$\varphi_v(\eta) = \varphi_w(\eta) + 2k(\eta)\pi \quad (13)$$

With:

$$k(n) = \begin{cases} 0, & \text{if } \varphi_w(n) - \varphi_w(\eta - 1) \leq \pi \\ +1, & \text{if } [\varphi_w(n) - \varphi_w(\eta - 1)] > -\pi \\ -1, & \text{if } [\varphi_w(n) - \varphi_w(\eta - 1)] < \pi \end{cases} \quad (14)$$

The algorithm (14) is encoded in Matlab by the "unwrap" function according to the Anderson technique, The phase unwrapping path according to this algorithm is unique and long, thus promoting the propagation of errors due to the noise mentioned above.

$\varphi_w(n)$	0.5000	0.6000	0.7000	0.8000	0.9000	0	0.1000	0.2000
$\varphi_w(n)_{bruité}$	0.5000	0.6000	0.7000	0.8000	3.9000	0	0.1000	0.2000
$k(n)$	0	0	0	0	1	1	1	1
$\varphi_v(n)$	0.5000	0.6000	0.7000	0.8000	3.9000	6.2832	6.3832	6.4832

Itoh's algorithm can be run in 2D by unfolding horizontally first. The resulting phase is then unfolded vertically. In this variant, the initial unfolding direction (horizontal or vertical) can be reversed.

Goldstein's 2D algorithm

The basic principle used by this algorithm remains the same as that of Itoh but with a two-dimensional approach developed by Goldstein. The difficulty lies in the fact that in 2D we are faced with several paths.

Thus, depending on the unfolding path followed, the final result will not always be the same. Also, it is necessary to find a mathematical artifice or something else to avoid any propagation of error during unfolding.

In summary, Goldstein's algorithm starts from an initial point and proceeds by integrating the folded phase on well-chosen paths using the notion of residues, whose pseudo-code is given in the book by Ghiglia and Pritt. If we denote by $\omega(n,m)$ the two-dimensional discrete phase, the residues are calculated in the following manner by referring to Figure 15:

$$\begin{aligned}\Delta_1 &= \varphi\omega(\eta + 1, m) \varphi\omega(n, m) \\ \Delta_2 &= \varphi\omega(n + 1, m + 1) \varphi\omega(n+1, m) \\ \Delta_3 &= \varphi\omega(n, m+1)(n+1, m + 1) \\ \Delta_4 &= \varphi\omega(n, m) \varphi\omega(n, m+1) \quad (15)\end{aligned}$$

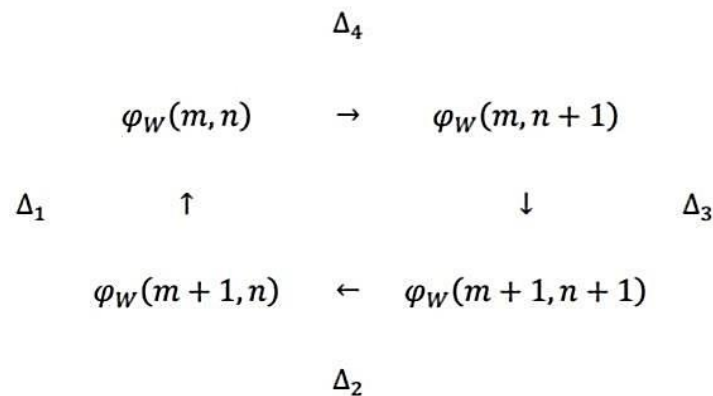


Figure 15. Calculation of residuals

Figure 15 shows how the residuals are calculated.

$$\Sigma = E [\sum_{j=1}^4 \Delta_j / 2\pi] \quad (16)$$

The number Σ called charge residues can only be 0, 1, or 1. For those passionate about mathematical rigor, they will find the demonstration of this result in reference

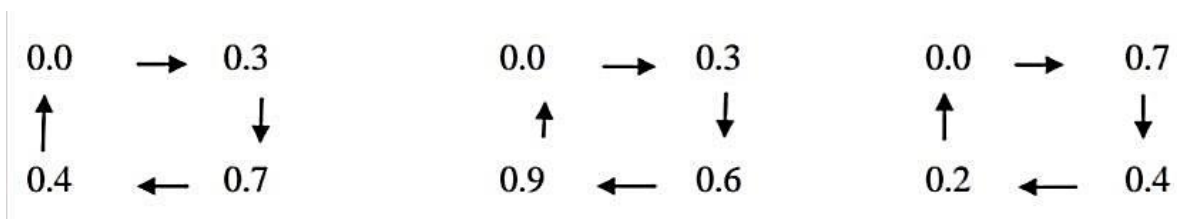
The basic idea of Goldstein's algorithm is as follows: When $[\Sigma]$ is equal to 1, between the four pixels concerned there is a noise that risks affecting the phase if it is taken into account in the unfolding procedure. Barriers must be placed on the unfolding path in such a way as to avoid the pixels giving rise to these singularities. In other words, the unfolding path must be chosen in the sense where the residual Σ is zero.

The arrangement of these barriers must be done by looking for the configuration that minimises the total length of these barriers. The barriers represent on the phase map the

segments of "defective" pixels that must be avoided in the unfolding procedure. The latter will be done quite simply by applying Itoh's algorithm.

Residues are associated with locations in the image where the aliased phase varies sharply and abruptly between two neighbouring pixels. This variation can only be related to local noise of any kind that manifests itself as an inconsistency with the phase values at neighbouring pixels.

Consider each of the following three sets of four pixels:



In the first group, the sum of the differences calculated in a clockwise direction is 0. In this case, we are therefore not in the presence of local noise since the number Σ is zero.

In the second group, the number Σ is +1, which shows the presence of a local error called positive residual. The last group leads to a residual of -1, thus showing the presence of a local error associated with a negative residual. When a positive or negative residual is introduced into a data set, it propagates and provides completely false unfolding results. To avoid this error propagation, it is not enough to exclude the pixels associated with the positive and negative residual, but to connect each positive residual (+1) to a negative residual (-1) by a barrier. During unfolding, we choose an integration path that does not cross barriers. (Appendix B includes an illustrative example of how this algorithm works).

Arevalillo Herráez 2D algorithm

This algorithm is based on the division of the map representing the folded phase distribution and the recursive use of the Itoh algorithm. The principle is relatively simple. It consists first in dividing the folded phase image into four square images, then unfolding them independently, and finally connecting them. To connect the images, the Itoh algorithm is applied to the pixels, forming the boundaries separating two contiguous unfolded images. This procedure is repeated until elementary images of size 2×2 pixels are reached.

The unfolding of an elementary image is very simple. One of the four pixels is chosen as a starting point and the Itoh algorithm is applied to the neighboring pixels in a cyclic sense. In Appendix (B), the diagram of the Arevalillo Herráez algorithm is given.

The test of the three algorithms discussed above will be carried out on the two-dimensional phase (Figure 16) whose expression is given by (1) and which has been folded using the $\arctan2(x)$ function of Matlab.

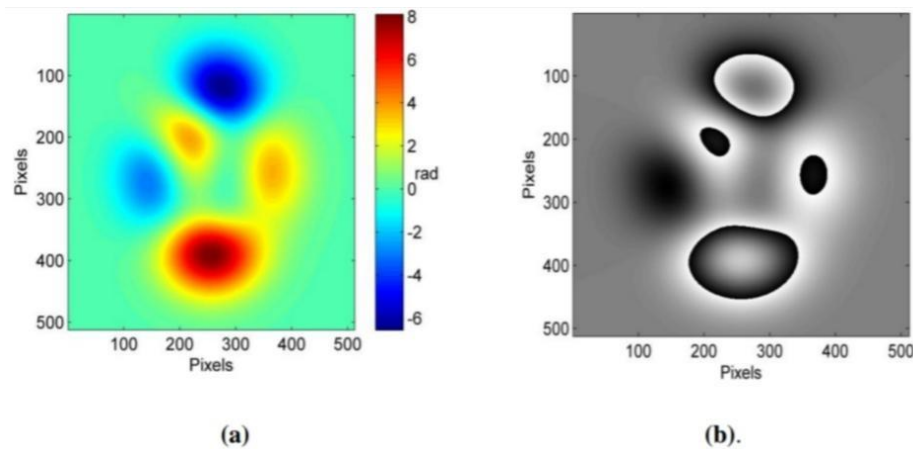


Figure 16. (a) Unfolded phase (b) Folded phase by calculating $\arctan2(x)$ of the unfolded phase.

Test without violation of the Itoh condition

Table 5 summarizes the test results of the three algorithms in terms of mean square error σ . It can be seen that if the signal to be unfolded varies slowly, in the sense that the phase differences between two contiguous pixels in a direction are less than π , the three algorithms manage to detect in the folded phase the discontinuities of mathematical origin as justified by the low value $\sigma \approx 0$ in Table 5.

Table 5. Mean square errors resulting from applying the three algorithms to unfold the phase of Figure 16 b.

	Itoh's algorithm		Goldstein's algorithm	Arevalillo Herráez algorithm
	1D	2D		
σ	3.910^{-16}	3.210^{-16}	7.710^{-3}	7.510^{-8}

Test with violation of Itoh's condition

To achieve such a situation, a linear profile reference phase was added to the initial phase. The result of this addition is shown in Figure 17. To better appreciate the effect of this addition, we considered a line of the phase image and applied it as an example to the Itoh ID algorithm to unfold the phrase. We note from the results represented by Figure 18 that adding a line of slope $2v$, too steep, will violate the Itoh condition and cause discontinuities to appear in the unfolded phase. This is clearly shown in Figure III-20 which gives the 2D mapping of the phase unfolded by the Itoh ID algorithm.

Table 6 compares the errors and the computation times to unfold the phase of the figure by the three algorithms studied. The 2D version of the Itoh algorithm allows to considerably improve the unfolding quality compared to the ID version. The use of the Arevalillo Herráez algorithm remains the most precise with a relatively short computation time. On the other hand, the Goldstein algorithm leads in this case to a less precise result than that of the 2D Itoh algorithm. This can be explained by the fact that the simulated phase

has only jumps in the horizontal direction. Thus, the residues can cancel each other out two by two, leading to very few barriers to unrolling the phase correctly.

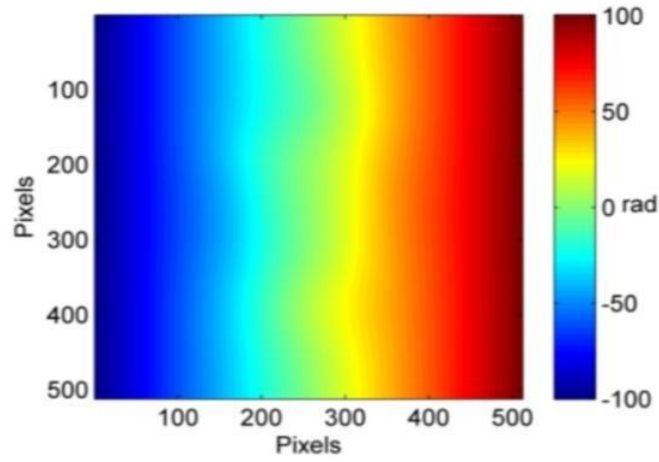


Figure 17: Unfolded Phase

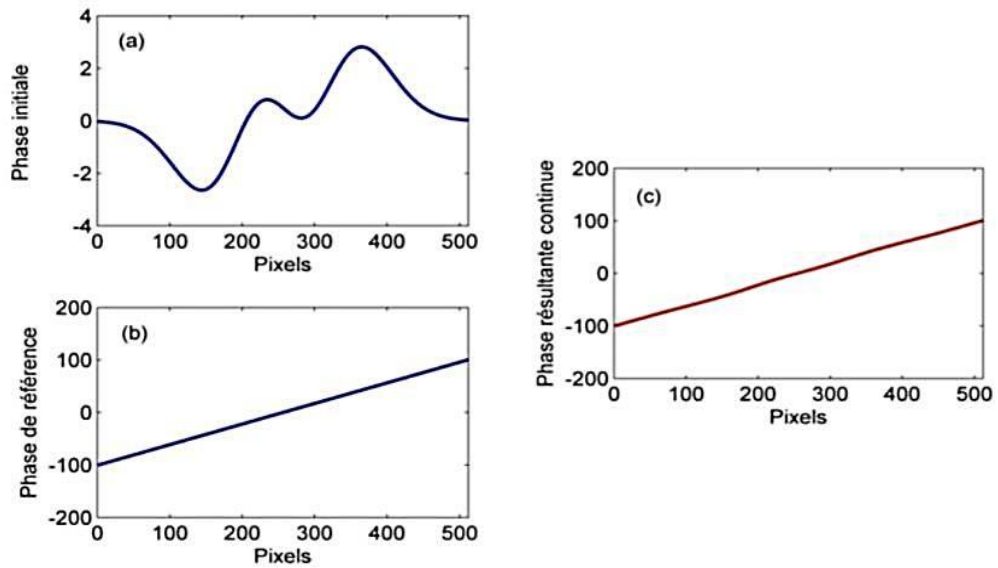


Figure 18. (a) Initial phase (b) linear phase (c) resultant phase

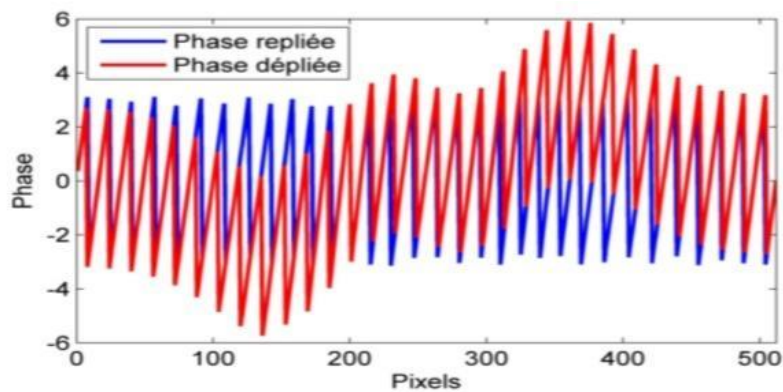
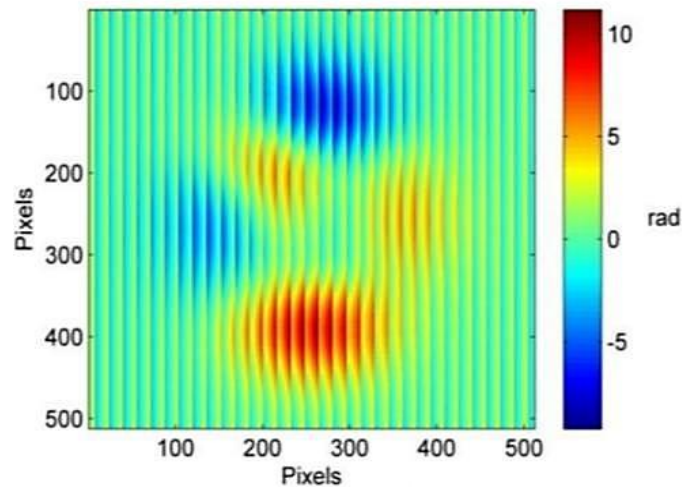


Figure 19. Phase unfolded by Itoh's algorithm which resembles the folded phase.**Figure 20.** Image of the phase unfolded by the Itoh ID algorithm**Table 6.** Root mean square deviation values and execution times on a laptop equipped with a 2Ghz Core™ 2 Duo microprocessor and 16GB SDRAM memory.
.GB size 4

Itoh's algorithm		Goldstein's algorithm	Arealillo Herráez algorithm
1D	2D		
115.9607	3,927	7.2373	0.3928
10^{-4}	1.0140s	67s	1.177s

Conclusion

This research concludes the inventory of our toolbox for the analysis of fringe images. The algorithms intended for this purpose have been explained and detailed by applying them to an image of fringes synthesized from an analytical expression.

Becoming an increasingly broad field of activity, it requires new means of control that are more efficient, more effective, and low cost. The most popular techniques in this field are largely based on sophisticated optical equipment such as Mach-Zehnder, Michelson, etc. On the other hand, the use of holographic interferometry and moiré deflectometry has made it possible to simplify the hardware as much as possible and to transfer the load to the intelligent and precise image processing algorithms offered by these techniques. The objective of this thesis is to develop a whole chain of algorithms allowing the tomographic reconstruction of the temperature field of an axisymmetric transparent medium. The entity of the study carried out consists in proposing at least three classes of algorithms allowing access to information on the temperature field tomography.

We have attributed a large part to the wavelet crest estimation algorithms. This led us to explain in a comparative manner three crest estimation algorithms: the direct maximum

algorithm, the Liu algorithm and finally the Marseille group algorithm. The calculation of the PSNR quality criterion reveals that the Liu algorithm is the most robust of the other two but this is at the expense of the computation time. This drawback led us to adopt the direct maximum algorithm which in our opinion achieves a compromise between precision and algorithmic complexity whether temporary or spatial.

Regarding the phase unfolding step, we have presented in a comparative manner three algorithms namely: the Itoh ID and 2D algorithm, the Goldstein 2D algorithm and the Herráez 2D algorithm. This comparison shows that the Herráez algorithm provides very good results.

References

- Asaki, T. J., Chartrand, R. Vixie, K. R & Wohlberg, K. R. "Abel inversion using total-variation regularization Inverse Problems, IOP Publishing, 2019,p30
- Bracewell, R. N. (2000). *The Fourier Transform and its Applications*, Boston: Third edition, McGraw-Hill International Editions.
- Camacho, J. R., Beg, F. N. & Lee, P. (2021). Comparison of sensitivities of Moire deflectometry and interferometry to measure electron densities in z-pinch plasmas, *Applied Physics*, p199
- Chan, C. Y G. & Hieftje, G. M. (2021). «A LabVIEW program for determining confidence intervals of Abel-inverted radial emission profiles,» *Spectrochimica Acta Part B*,p14
- Choi, G. (2024). Optimization study of a probe chuck for semiconductor wafers using genetic algorithm and deep reinforcement learnings. *Journal of Mechanical Science and Technology*. <https://doi.org/10.1007/s12206-024-0734-4>
- Dribinski, V., Ossadtchi, A., Mandelshtam, V & Reisler, H. «Reconstruction of Abel-transformable images: the Gaussian basis-set expansion Abel transform method,» *Review of Scientific Instruments*, 2020,p55
- Federico, A., Kaufmann. G (2021), «Phase retrieval in electronic speckle interferometry using the continuous wavelet transform, SAR Image Analysis, Modeling, and Techniques,p121
- Goharkhaha, M., Ashjaee, M & Madanipour, K. (2020). «Investigation of the accuracy of different methods of interferogram analysis for calculation of local free convection heat transfer coefficient on axisymmetric objects,»>>> *Experimental Thermal and Fluid Science*, p111
- Ignjatovic, K. M., & Mihajlov, A.A , «The realization of Abel's inversion in the case of discharge with undetermined radius,» *Journal of Quantitative Spectroscopy & Radiative Transfere*, 2019,p79
- Jackson, S. L. & Shumlak, U. (2021). «Abel inversion of a holographic interferogram for determination of the density profile of a sheared-flow Z pinch,»>> *Review Of Scientific Instruments*, p21

- Junne, H. (2024). Rainbow Schlieren Deflectometry for spherical fields: A new algorithm and numerical validation approach. *Numerical Heat Transfer, Part B: Fundamentals*, 85(9), 1178–1201. <https://doi.org/10.1080/10407790.2023.2262124>
- Li, H. (2024). Numerical algorithm with fifth-order accuracy for axisymmetric Laplace equation with linear boundary value problem. *Numerical Methods for Partial Differential Equations*, 40(3). <https://doi.org/10.1002/num.23079>
- Liu, H., Cartwright, A & Basaran, C. «Moiré interferogram phase extraction: a ridge detection algorithm for continuous wavelet transforms,» *Applied Optics*, 2020,p58
- Liu, Y. (2024a). Simultaneous Identification of Thermophysical Properties of Semitransparent Media Using a Hybrid Model Based on Artificial Neural Network and Evolutionary Algorithm. *Transactions of Nanjing University of Aeronautics and Astronautics*, 41(4), 458–475. <https://doi.org/10.16356/j.1005-1120.2024.04.004>
- Liu, Y. (2024b). Structural Optimization of a Giant Magnetostrictive Actuator Based on BP-NSGA-II Algorithm. *Actuators*, 13(8). <https://doi.org/10.3390/act13080293>
- Lv, J. (2024). Optimization design of forebody shape of an underwater axisymmetric body for transition delay using a genetic algorithm. *Ocean Engineering*, 301. <https://doi.org/10.1016/j.oceaneng.2024.117529>
- Maddah, A. (2024). Optimizing die profiles using a hybrid optimization algorithm for the precise control of extrudate swell in polymer solutions. *Journal of Non-Newtonian Fluid Mechanics*, 330. <https://doi.org/10.1016/j.jnnfm.2024.105277>
- Motassadeq, A. (2020). Contribution to the valorization of optical shearography and deflectometry techniques for measuring the temperature field in a semi-transparent medium with axial symmetry, FSTG Marrakech,p179
- Sharma, G. (2024). Skin-Friction Topology on Axisymmetric Boattail Models by an Optical-Flow Algorithm with a Sub-grid Function. *Lecture Notes in Electrical Engineering*, 1050, 189–198. https://doi.org/10.1007/978-981-97-3998-1_16
- Yu, B. (2024). Optimal design of a clamp band system based on genetic algorithm and experimental verification. *Aerospace Science and Technology*, 145. <https://doi.org/10.1016/j.ast.2024.108870>
- Zarch, A. B. (2024). Hybrid Algorithm for Development of Reduced Skeletal Kinetic Mechanisms with Specific Species Targeting. *ACS Omega*, 9(8), 9123–9136. <https://doi.org/10.1021/acsomega.3c07936>
- Zhong, Z. W., Lu, Y. G. (2019). «Measurements of surface deformations and strains using an AFM moiré method,» *Measurement*, p183